APPLIED SCIENCES AND ENGINEERING

Realization of 2D crystalline metal nitrides via selective atomic substitution

Jun Cao[1]*, Tianshu Li[2]*, Hongze Gao[2], Yuxuan Lin[3], Xingzhi Wang[1], Haozhe Wang[3], Tomás Palacios[3], Xi Ling[1,2,4]†

Two-dimensional (2D) transition metal nitrides (TMNs) are new members in the 2D materials family with a wide range of applications. Particularly, highly crystalline and large area thin films of TMNs are desirable for applications in electronic and optoelectronic devices; however, the synthesis of these TMNs has not yet been achieved. Here, we report the synthesis of few-nanometer thin Mo_5N_6 crystals with large area and high quality via in situ chemical conversion of layered MoS_2 crystals. The versatility of this general approach is demonstrated by expanding the method to synthesize W_5N_6 and TiN. Our strategy offers a new direction for preparing 2D TMNs with desirable characteristics, opening a door for studying fundamental physics and facilitating the development of next-generation electronics.

INTRODUCTION

Transition metal nitrides (TMNs) are well-known for their high melting points, hardness, and chemical inertness (*1, 2*). The successful preparation of two-dimensional (2D) MXenes through selectively etching the "A" layer of bulk MAX phase triggered the study of 2D metal carbides and nitrides since 2011 (*3–6*). Although a variety of carbide MXenes have been synthesized using this method, the synthesis of nitrides MXenes is limited to Ti_4N_3 and Ti_2N (*7, 8*), due to the low availability of bulk MAXs for corresponding 2D metal nitrides. Urbankowski *et al.* (*9*) further reported the synthesis of multilayer molybdenum and vanadium nitrides by ammonation of carbide MXenes synthesized using the selective etching method. Currently, as-synthesized 2D TMNs are either in solution phase or in powder form, and the lateral sizes of the flakes are usually small (<10 μm) (*10–15*). In addition, samples prepared by selective etching suffer from defects generated during the etching process and large thickness distributions (*16, 17*). These types of 2D TMNs are not suitable for high-performance electronic and optoelectronic device applications, which often require 2D crystals with decent area (>10 μm of lateral size), quality, and deposition on solid-state substrates (*18, 19*). Conventional 2D materials such as graphene and transition metal dichalcogenides (TMDs) produced using chemical vapor deposition (CVD) have made substantial progress in advancing the development of electronic devices (*20–22*). In contrast to many conventional 2D materials with strong in-plane covalent bonds and weak out-of-plane van der Waals interactions between the layers, the van der Waals gap is absent in bulk TMN crystals. Instead, covalent bonding extends in 3D frameworks of TMNs. Thus, conventional methods such as top-down mechanical exfoliation and bottom-up CVD, which take advantage of the weak interlayer van der Waals interaction and self-limited in-plane growth, are ineffective for the synthesis of large-area and ultrathin 2D TMNs. Therefore, developing effective routes to synthesize 2D TMN crystals with desired morphology and quality is essential to realize the potential for applications toward electronic devices.

Using nitriding reaction of metal oxides, TMDs, and transition metal carbides (TMCs) to synthesize bulk TMNs is an established process (*23–28*). Recently, transformation of 2D MoS_2 and TMCs to 2D TMNs while retaining crystal structure was demonstrated in an ammonia atmosphere (*9, 27*). This transformation method is promising for large-area synthesis of 2D TMNs, considering the well-established preparation methods of TMD thin films with controlled thickness and various lateral dimensions ranging from micrometer size to wafer scale (*22, 29, 30*). However, the precursors used in the reported work for the transformation are either multilayered carbide MXenes or powder TMDs (*9, 27*). The obtained 2D TMNs are still marred by large thickness distributions, defective structures, and small lateral sizes passed on from the precursors. Moreover, an atomic-level investigation of the transformation, which is the key to evaluate the potential of the strategy for producing high-quality and large-area 2D TMN crystals, is lacking.

Here, beginning with a precursor layer of MoS_2, an in situ transformation from MoS_2 to ultrathin Mo_5N_6 is achieved. Optical and scanning electron microscopy (SEM) images show that the geometry and morphology of the crystals are retained during the transformation. The obtained Mo_5N_6 exhibits high crystallinity over the entire area. In situ transformations of various MoS_2 flakes down to four layers for Mo_5N_6 flakes with different thicknesses are achieved. Atomic force microscopy (AFM) analysis shows that the thickness of most of MoS_2 flakes is reduced by about two-third after the transformation. Electrical measurements show the high conductivity of metallic Mo_5N_6 samples. We further demonstrate that this strategy can be applied to other TMDs such as WS_2 and TiS_2 for preparing their corresponding TMNs. This work opens a new direction for preparing 2D TMNs with desired quality that are previously inaccessible.

[1]Department of Chemistry, Boston University, 590 Commonwealth Avenue, Boston, MA 02215, USA. [2]Division of Materials Science and Engineering, Boston University, 15 St. Mary's Street, Boston, MA 02215, USA. [3]Department of Electrical Engineering and Computer Science, Massachusetts Institute of Technology, Cambridge, MA 02139, USA. [4]The Photonics Center, Boston University, 8 St. Mary's Street, Boston, MA 02215, USA.
*These authors contributed equally to this work.
†Corresponding author. Email: xiling@bu.edu

RESULTS

Figure 1 shows a schematic illustration of the typical reaction process. The conversion was performed in a horizontal tube furnace

(see Materials and Methods for details of synthesis). MoS_2 flakes with different thicknesses were prepared using mechanical exfoliation and transferred onto a SiO_2/Si substrate, which was then placed at the center of the furnace. A crucible filled with urea was placed in the upstream zone of the furnace, serving as the ammonia gas source, which was released from the thermolysis of urea at 200°C (31, 32). Ar gas (100 sccm) was used as carrier gas. The temperature in the center of the furnace was set at 750° to 800°C for the chemical reaction between gaseous ammonia and MoS_2 flakes (23, 27). Apart from Mo_5N_6, which was the solid product, the other two side products, H_2S and N_2, were in gaseous phase and carried away by the Ar gas (23, 27), leaving clean Mo_5N_6 products with minimum contaminants.

Figure 2 (A and B) shows optical images of a 12.9-nm MoS_2 flake before and after the reaction. The optical contrast of the flake changed markedly after the reaction, but the morphology and shape of flakes are retained. Conversion results of more MoS_2 flakes with different thicknesses ranging from ~3 nm to tens of nanometers are shown in fig. S1. All MoS_2 flakes displayed notable changes of optical contrast after conversion. Absorption spectra (fig. S2) of the flake before (MoS_2) and after (Mo_5N_6) the conversion suggest that such change originated from the distinct optical properties, consistent with the distinct electronic band structures of the two materials (15, 33). More evidence supporting the successful conversion of MoS_2 to Mo_5N_6 is reported in later sections. AFM images show the atomically smooth surface of the flakes after conversion (fig. S3), suggesting a mild conversion process during which the reaction is confined within the original MoS_2 flakes. We further measured the Raman and photoluminescence (PL) spectra of the flake before and after the chemical transformation. As shown in Fig. 2C, pronounced A_{1g} and E^1_{2g} modes at ~384 and ~407 cm^{-1} (34, 35) were observed from MoS_2 flakes before the transformation. Both modes vanished completely after the reaction, and new Raman peaks at ~215 and 710 cm^{-1} appeared, indicating the transformation of the crystal domain. Similarly, PL from MoS_2 disappeared after the conversion (Fig. 2D) (33, 36), matching well with the semiconducting and metallic property of MoS_2 and Mo_5N_6 (15, 33). In addition, Raman mapping results (Fig. 2, E and F) indicated that the entire flake was converted from MoS_2 to Mo_5N_6, where no Raman signals from MoS_2 were observed

on the converted flake globally. Corresponding PL mapping results are shown in fig. S4.

To determine the phase and crystal structure of the flake, we performed transmission electron microscopy (TEM) characterization on an as-prepared sample. The low-magnification TEM image in Fig. 3A shows the smooth surface of the flake where the small variations of the contrast are due to the wrinkles generated during the transfer process. The selected-area electron diffraction (SAED) pattern in Fig. 3B (see also fig. S5) indicates the high crystallinity of the sample. Same SAED pattern was observed when measuring on different regions of the flake. The hexagonal diffraction pattern is consistent with the crystal structure of the Mo_5N_6 (15). The experimental and simulated SAED patterns (fig. S5) of Mo_5N_6 match well with each other. High-angle annular dark-field (HAADF) scanning transmission electron microscopy (STEM) image is shown in Fig. 3C, where Mo atoms and atomic lattice are seen and no obvious defect is found in the sample. N atoms are invisible under our STEM condition due to the small atomic number compared to Mo atoms. In addition, the distance of 0.239 nm between the lattice planes is consistent with the d-spacing of (110) planes in Mo_5N_6 crystal, which matches with the SAED pattern. We also noticed that the obtained Mo_5N_6 crystal had an enhanced stability under 200-keV electron beam compared to MoS_2 flakes (37, 38), where Mo_5N_6 flakes on TEM grid remained stable without noticeable change after being exposed under electron beam for 30 min (fig. S6), providing an additional advantage for future applications in electronic devices. STEM imaging and energy-dispersive spectroscopy (EDS) mapping were performed (see fig. S5) on a thick Mo_5N_6 flake, which provides better signal-to-noise ratio of EDS signal. Dark-field STEM image shows the inhomogeneous contrast of the thick Mo_5N_6 flake (fig. S5), which is probably due to strong local strain during the conversion process. EDS maps of N K peak and Mo L peak (fig. S5) show uniform distribution of Mo and N elements in the flake. The TEM characterization confirmed that a highly crystalline Mo_5N_6 flake was successfully obtained through the chemical transformation.

The chemical composition and oxidation states of the elements in sample Mo_5N_6 were characterized using x-ray photoelectron spectroscopy (XPS) and EDS analyses. Figure 3D shows the XPS wide scan survey spectrum of the sample, where notable Mo and
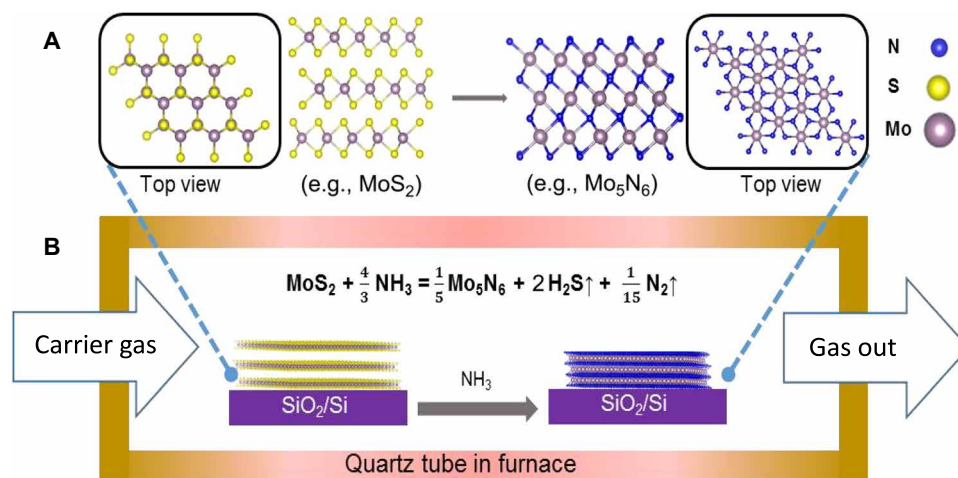
Fig. 1. Schematic illustration of chemical conversion from MoS_2 to Mo_5N_6. (A) Structural changes from MoS_2 to Mo_5N_6. (B) Schematics of the experimental setup for chemical conversion reactions.
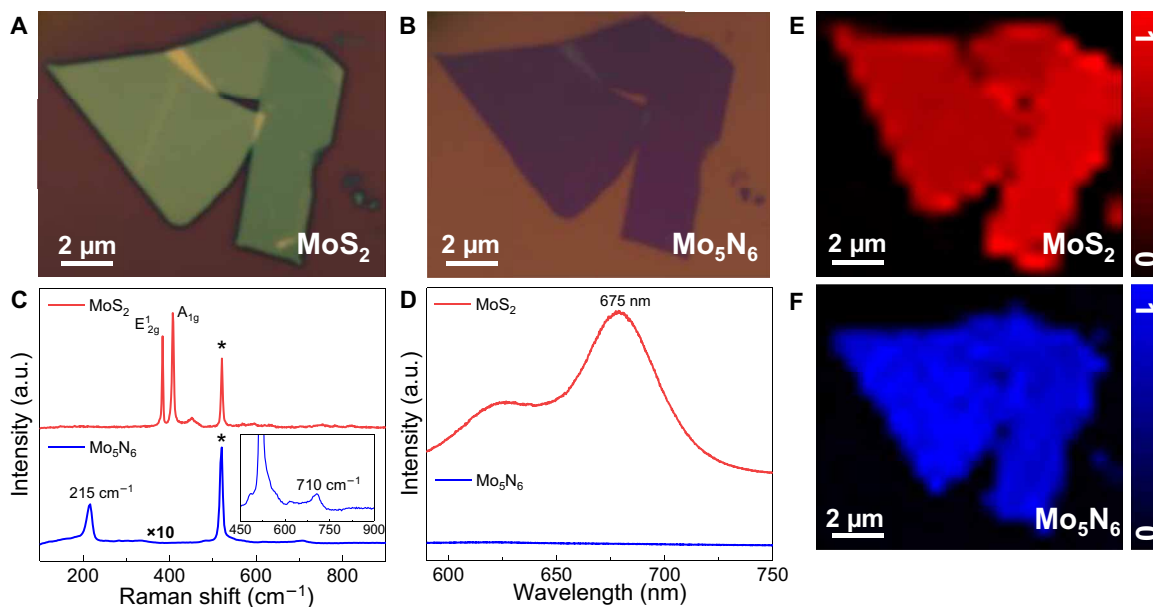
Fig. 2. Typical optical microscope, Raman spectroscopy, and PL characterization of MoS₂ and Mo₅N₆ flakes. (**A**) Optical images of MoS_2 exfoliated on the SiO_2/Si substrate. (**B**) Optical image of Mo_5N_6 converted from MoS_2 in (A). (**C**) Comparison of Raman spectra of MoS_2 and Mo_5N_6. Peaks labeled with "*" are from the SiO_2/Si substrate. (**D**) Comparison of PL spectra of MoS_2 and Mo_5N_6. (**E** and **F**) Raman intensity maps of the A_{1g} mode of MoS_2 (E) and the 215 cm^{-1} mode of Mo_5N_6 (F). Color bars show normalized Raman intensities, where "1" and "0" represent maximum and minimum intensity of Raman modes, respectively. a.u., arbitrary units.
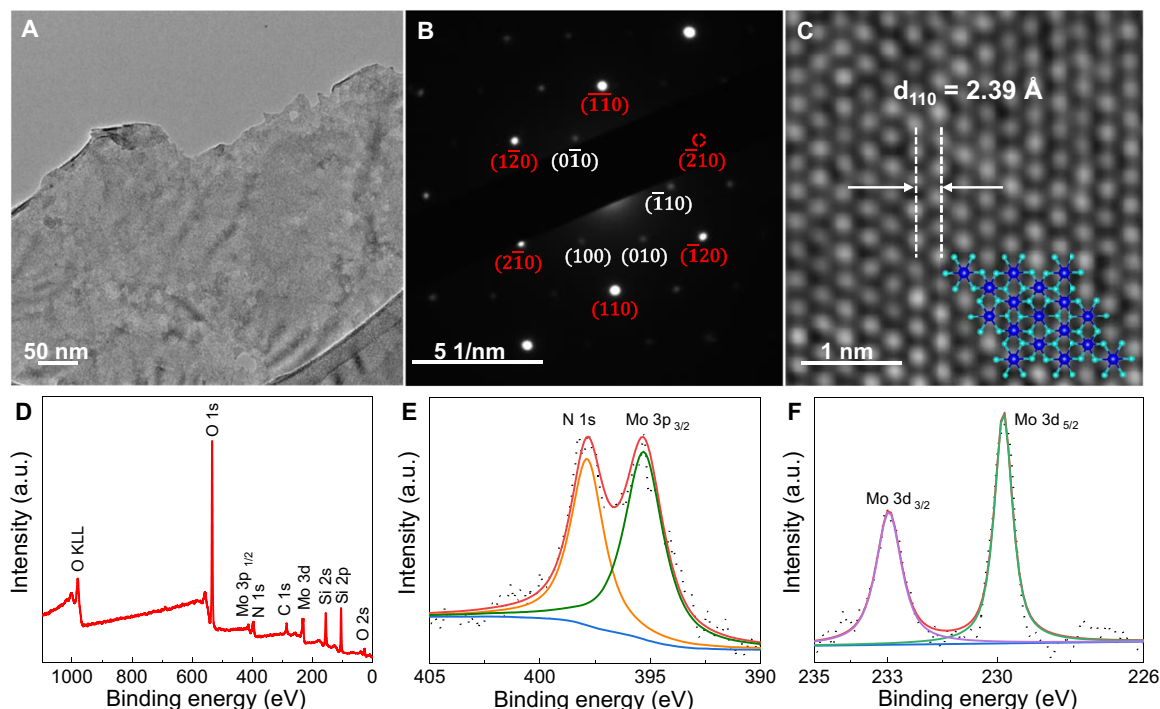
Fig. 3. Crystal structure and elemental analysis of Mo₅N₆ samples converted from MoS₂. (**A**) Low-magnification TEM image of Mo_5N_6. (**B**) SAED pattern taken by a 25 cm camera. Diffraction planes are labeled according to SAED simulation in fig. S4. Red circle corresponds to a diffraction plane blocked by TEM beam stop. (**C**) Filtered HAADF STEM image. Hexagonal Mo pattern is observed. Mo atoms and N atoms are labeled in blue and cyan color, respectively. (**D**) XPS survey spectrum of Mo_5N_6. (**E** and **F**) XPS spectra of Mo_5N_6 in Mo 3p and N 1s region (E) and Mo 3d region (F).

N signals are observed and no signal from S appeared, indicating complete conversion of MoS_2 to Mo_5N_6. Other elements such as O, Si, and C are from the SiO_2/Si substrate and the chamber environment. Similar results were obtained from EDS characterization (fig. S7).

High-resolution XPS spectra deconvolution for N 1s, Mo 3p, and Mo 3d regions are shown in Fig. 3 (E and F). The N 1s peak at 397.9 eV and Mo 3p $_{3/2}$ at 395.3 eV (Fig. 3E) suggest that chemical bond formed between Mo and N (*15*). In the Mo 3d region (Fig. 3F),

the peaks at 233.0 and 229.8 eV were assigned to the binding energies of Mo 3d $_{3/2}$ and Mo 3d $_{5/2}$, respectively (*39*), with a spin-orbit splitting of 3.2 eV. This characteristic doublet of core-level Mo 3d $_{5/2}$ and 3d $_{3/2}$ indicates that Mo (+4) oxidation state dominates in Mo_5N_6 (*25*). Nevertheless, the binding energy of 229.8 eV is slightly smaller than the reported value at 230.0 eV for Mo (+4) oxidation state (*15*), suggesting the coexistence of Mo (+3) oxidation state in the sample. No peaks corresponding to higher oxidation states of Mo from MoO_x were observed in the Mo 3d region (*40*), ruling out the possibility of the formation of MoO_x.

To address the mechanism by which the lattice changed during the atomic substitution from MoS_2 to Mo_5N_6, we investigated thickness changes of flakes before and after chemical conversion. The crystal structure models of MoS_2 and Mo_5N_6 (Fig. 4, A and B) predict that the van der Waals gap between MoS_2 layers will disappear during the transformation to Mo_5N_6 crystals, leading to the reducing of the thickness from MoS_2 to Mo_5N_6. The distance between two Mo layers in MoS_2 is 7.66 Å (*41*), while it is 2.77 Å in Mo_5N_6 (*42*); therefore, the thickness of the flake can be predicted to decrease to 36% when transforming from MoS_2 to Mo_5N_6. To test this hypothesis, we performed AFM to extract the thickness of flakes. As expected, we observed that the thickness was reduced after chemical transformation. Figure 4 (C and D) shows typical AFM images of MoS_2 and corresponding Mo_5N_6 flake, where they have nearly the same morphology and both surfaces are smooth. However, the thickness of the flake decreased from 9.5 nm for MoS_2 to 3.5 nm for Mo_5N_6 (Fig. 4E), where Mo_5N_6/MoS_2 thickness ratio is 37%. Furthermore, we performed this comparison for ~30 flakes with MoS_2 thickness ranging from a few nanometers to ~35 nm. Reduced sample thickness was observed for all flakes after conversion (Fig. 4F). The average Mo_5N_6/MoS_2 thickness ratio is 56% based on the slope of linear fitting curve, but for

MoS_2 flakes with the thickness of 5 to15 nm, the ratio is around 40%, matching well with the expected value. For thinner flakes, the ratio is larger, probably because the termination groups on the surface are non-negligible at this size range (*3*, *5*) or the substrate roughness introduces a large uncertainty for the measurement. Figure S8 shows that a four-layer MoS_2 flake (3.4 nm) turned to a 2.1 nm Mo_5N_6 flake after conversion. Note that we found that the morphology and quality of the flake remain well at such thin level. On the basis of the morphology retaining and thickness depression phenomena observed in our experiments, we propose the following mechanism of the chemical transformation from MoS_2 to Mo_5N_6. When NH_3 gas diffuses into the van der Waals gaps of the MoS_2 flake, one N atom will replace two S atoms sandwiched by two adjacent Mo layers. When Mo—S bonds around a Mo atom are broken, six binding sites on the Mo atom will be released. Each N atom will then bond with six Mo atoms to form Mo_5N_6, where adjacent Mo layers are bridged by the N atoms, leading to the vanishing of the van der Waals gaps that originally exist in MoS_2. In this process, breaking Mo—S bonds and forming Mo—N bonds do not require large rearrangements of Mo atoms, although small shift of positions of Mo atoms may be necessary to compensate the bond length difference between Mo—S and Mo—N. Despite the layered structure of MoS_2 (point group, D_{6h}; space group, $P6_3/mmc$) (*41*) and nonlayered nature of Mo_5N_6 (point group, C_{6h}; space group, $P6_3/m$) (*42*), the Mo layers in these two materials are both in hexagonal pattern. This similarity in structure allows gentle transformation without structural collapse, leading to the morphology retaining of samples before and after chemical transformation.

To further investigate the transformation process, we performed the reaction under varying conditions. We found that excess amount of urea, which provided sufficient NH_3 gas in the chamber, was a
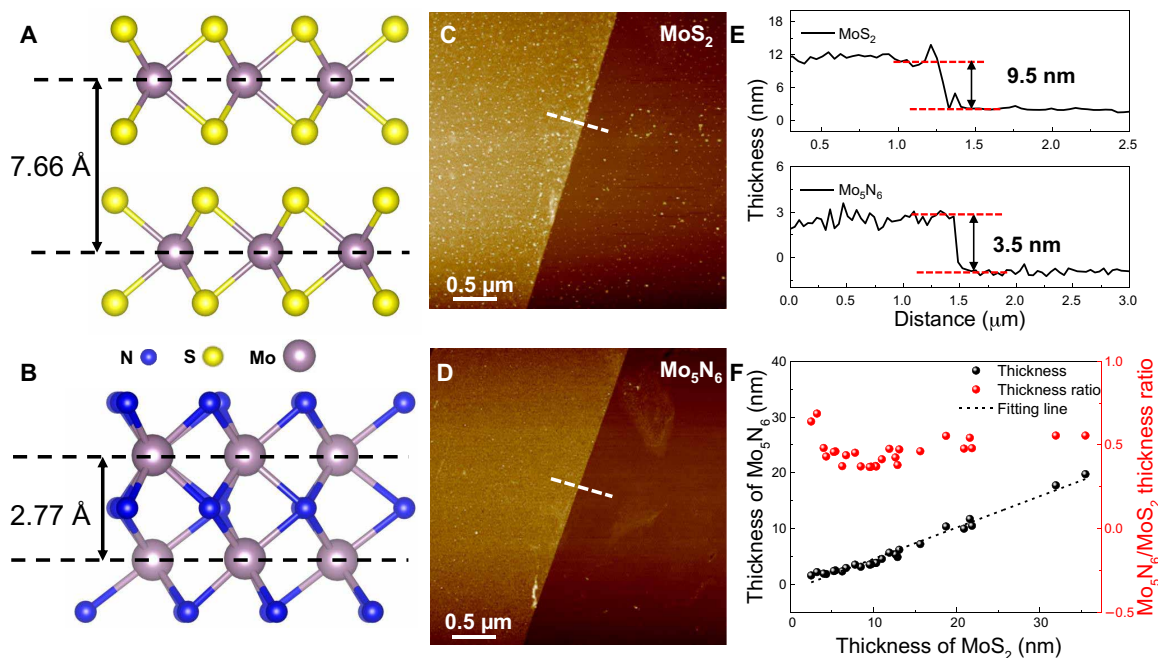
Fig. 4. Thickness characterization and analysis of samples before (MoS_2) and after conversion (Mo_5N_6). (**A** and **B**) Side view of crystal structures labeled with distance between adjacent Mo layers in MoS_2 and Mo_5N_6. (**C** and **D**) AFM images of the same flake before [MoS_2 (C)] and after conversion [Mo_5N_6 (D)]. The white dashed lines indicate the location where we measured the thickness of the flakes. (**E**) AFM height profiles of the flake before [MoS_2 (C)] and after conversion [Mo_5N_6 (D)]. (**F**) Correlation plot of the thickness of MoS_2 and converted Mo_5N_6 (in black). Data points in red show the corresponding thickness ratios of Mo_5N_6/MoS_2.

key factor for the success because it ensured a reducing environment to prevent MoS_2 from oxidation (fig. S9). In addition, the degree of conversion could be tuned by changing the reaction temperature and time. A complete conversion occurred within 5 min when the reaction temperature varied from 750° to 800°C (fig. S9). However, at 700°C, the conversion was only partially complete even after 60 min, where only the edge area was converted and no Mo_5N_6 was observed in the central region of the flake (fig. S10), indicating that the conversion started from the edge of the MoS_2 flake. Because of the partial conversion, we realized a lateral heterostructure between MoS_2 and Mo_5N_6 through a simple partial conversion. The successful synthesis of this heterostructure offers a great platform for future study on the junction properties and applications. Moreover, the converted Mo_5N_6 showed excellent stability, where the crystal structure remained intact after 6 months and survived in acetone, deionized (DI) water, and 1 M H_2SO_4 solution for at least 2 hours without noticeable changes from optical images and Raman spectra (fig. S11). This is advantageous to be compatible with future device fabrication process.

To examine the electrical property of the converted Mo_5N_6 sample, we fabricated a back-gate transport device on a 9.5 nm-thick Mo_5N_6 flake (Fig. 5A and fig. S13). The gate dependence of the transport current shows that the drain-source current (I_{ds}) remained constant as the gate voltage scanned from −20 to 20 V, and variations of I_{ds} was still negligible even when noise signal became visible, featuring metallic behavior of the as-synthesized Mo_5N_6 sample (Fig. 5B). We further performed the temperature-dependent transport measurement down to 77 K to investigate the electrical conductivity of the sample. Fig. 5C shows the output current-voltage relation (I-V) characteristics through a four-probe measurement, where the slope of the

I-V curves increases very slowly as the temperature increases from 77 to 240 K (Fig. 5C, inset). The sheet resistances of Mo_5N_6 at different temperatures were extracted from the slope of I-V curves and the dimension of the transport device (Fig. 5D), using the formula $R_s = R \times (W/L)$. R is the total electrical resistance of the device, and W and L are the effective width and length of the measurement area, which are measured as 3.4 and 6.1 μm, respectively, from the optical image. Low sheet resistances of Mo_5N_6 ranging from 114.4 to 117.8 ohm square^{-1} were obtained under different temperatures, which is in the same order of magnitude of CVD graphene (43). The fact that the sheet resistance of Mo_5N_6 is not sensitive to the temperature change from 77 and 240 K is consistent with the trend of TMNs reported in the literature (9).

We further applied this strategy to the conversion from WS_2 and TiS_2 to their corresponding nitrides (see Materials and Methods for details of the synthetic conditions). Figure 6 shows a typical conversion result on a 5.6 nm WS_2 and a ~100 nm TiS_2 flake. As shown in Fig. 6 (A to H), distinct optical contrast change was observed from WS_2 and W_5N_6, as well as from TiS_2 to TiN. Similar to the case of MoS_2 to Mo_5N_6 conversion, the morphology of the flakes was retained. Raman characterization showed that the Raman signatures from WS_2 and TiS_2 disappeared completely (44, 45). Instead, new peaks that correspond to the phonon modes of W_5N_6 (e.g., ~258 cm^{-1}) and TiN (e.g., ~154 and 620 cm^{-1}) (46, 47) appeared (Fig. 6, I to J), indicating a successful chemical conversion. The Raman mapping results show that the conversion is thorough and uniform. More optical and corresponding SEM images of W_5N_6 (fig. S12) and TiN (fig. S12) corroborate uniform surface of converted samples. Phase and crystallinity of W_5N_6 are characterized by HRTEM and EDS analyses (fig. S14) (48). Similar to Mo_5N_6, W_5N_6 and TiN also exhibit
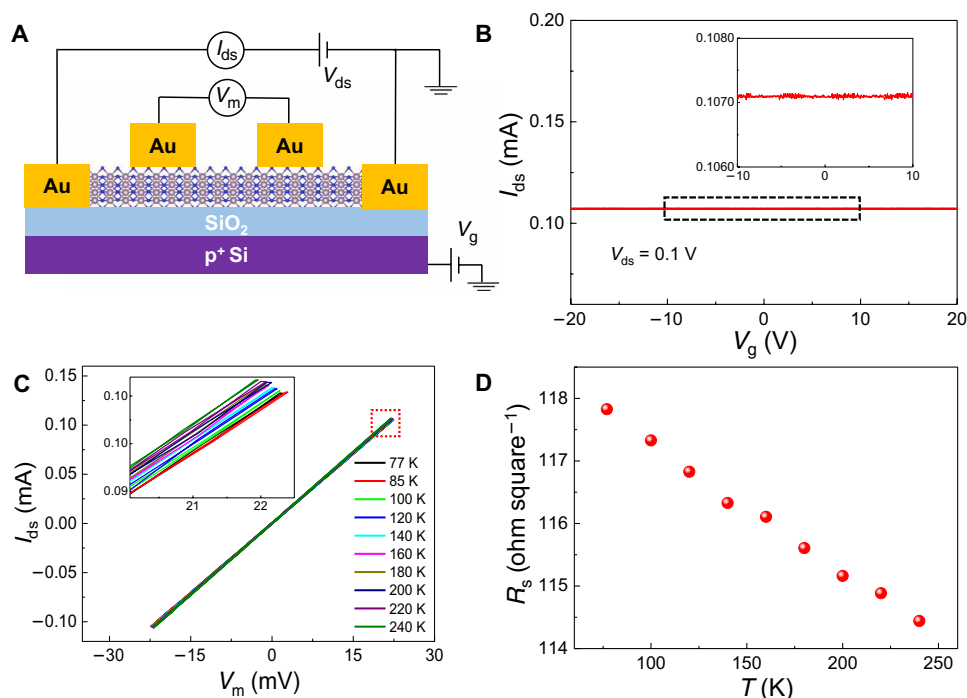
Fig. 5. Electrical transport measurements of Mo_5N_6. (**A**) Schematics of a back-gate device together with electrical connections. (**B**) Transfer curve of Mo_5N_6 transport device for both forward and reverse V_g bias with back-gate modulations. Inset: Zoomed-in image of the area indicated by the black rectangle. Negligible gate dependence of the I_{ds} is observed in Mo_5N_6 transport device. (**C**) Output I-V curve of Mo_5N_6 transport device under different temperatures at zero gate voltage. Inset: Zoomed-in region of the I-V curve indicated by the red square. (**D**) Temperature dependence of the sheet resistance of the Mo_5N_6 sample.

excellent stability against acetone, DI water, and 1 M H_2SO_4 for at least 2 hours (fig. S11).

DISCUSSION

We demonstrate a versatile conversion strategy from layered TMDs to their corresponding ultrathin nitrides through atomic substitution from chalcogen to nitrogen. This method facilitates the production of 2D crystalline TMNs including Mo_5N_6, W_5N_6, and TiN, offering a pathway toward an important class of 2D materials that previously are inaccessible. The investigation of the in situ transformation from MoS_2 layers to 2D Mo_5N_6 crystals shows reduced thickness after conversion. 2D Mo_5N_6 crystal as thin as 2.1 nm is achieved by converting a four-layer MoS_2. The electrical measurement shows that the converted Mo_5N_6 is metallic with high conductivity, where the sheet resistance is as low as 100 ohm square^{-1}. By controlling the reaction rate, we achieve a Mo_5N_6-MoS_2 lateral heterostructure, demonstrating the advantage of our method in integrating 2D materials together for basic building blocks (e.g., metal-semiconductor junction) for future applications in electronic devices. Building on

the success of the TMDs synthesis in the field (21, 22, 30), we anticipate that the strategy we report here will lead to effective synthesis of large-area and high-quality 2D TMNs that satisfy the needs for high-performance electronic and optoelectronic devices.

MATERIALS AND METHODS
Conversion from TMDs to TMNs

MoS_2, WS_2, and TiS_2 with different thicknesses were prepared using mechanical exfoliation method from their bulk crystals (purchased from HQ Graphene) and transferred onto 300 nm SiO_2/Si substrates. Note that SiO_2/Si substrates were cleaned by sonication in water, acetone, and isopropanol solvents sequentially (each for 10 min), followed by O_2 plasma cleaning before use. Chemical conversions were conducted in a horizontal tube furnace where Ar gas was introduced into the tube and the flow was controlled by a mass flow controller. Samples were placed in a 2.5-cm-diameter quartz tube in the center of the furnace. Excess amount of urea (500 mg) was placed in an Al_2O_3 crucible located upstream of the furnace, serving as nitrogen source. After purging with Ar gas for 10 mins, the tube was heated
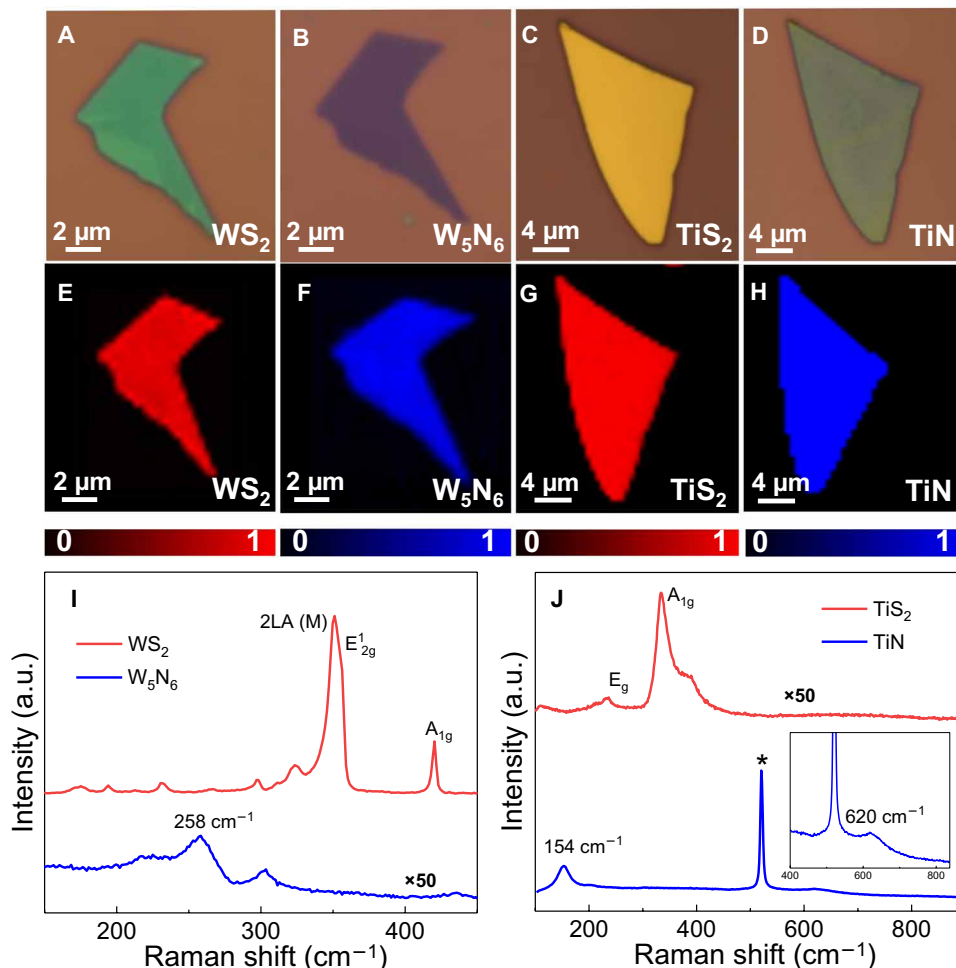
Fig. 6. Conversion on WS_2 and TiS_2 for W_5N_6 and TiN. (**A** to **D**) Optical images of WS_2 (A), W_5N_6 (B), TiS_2 (C), and TiN (D). (**E** to **H**) Raman intensity maps of E^1_{2g} mode of WS_2 (E), 258 cm^{-1} mode of W_5N_6 (F), A_{1g} mode of TiS_2 (G), and 154 cm^{-1} mode of TiN (H). Color bars show normalized Raman intensities, where "1" and "0" represent maximum and minimum intensity of Raman modes, respectively. (**I** and **J**) Comparison of Raman spectra of WS_2 and W_5N_6 (I) and TiS_2 and TiN (J). Peak labeled with "*" is from the SiO_2/Si substrate.

to 800°C with a 30 min ramp. The conversion time for Mo_5N_6 and TiN is 1 and 2 hours for W_5N_6. Throughout the conversion, 100 sccm Ar flow was used to maintain the inert atmosphere. When conversion was completed, the system was cooled down naturally.

Material characterizations

As-prepared TMNs were characterized using Raman spectroscopy, AFM, TEM, STEM, SAED XPS, and EDS. Raman and PL measurements were performed on a Renishaw inVia Raman microscope equipped with a 532 nm laser line. All the spectra in comparison were taken using the same condition. The AFM topography was acquired on a Bruker Dimension system. TEM measurements were performed on a FEI Tecnai Osiris TEM, operating at a 200 keV accelerating voltage. SAED was measured on a JEOL 2100 TEM. The SAED simulation was performed through STEM_CELL software (49). Atomic-resolution STEM and EDS mapping was performed on a JEOL ARM 200F STEM, operating at 200 keV. XPS measurements were performed using a PHI Versaprobe II.

Fabrication and conductivity measurements

The electrical transport device was fabricated through laser writer lithography and thermal evaporation of 5 nm Cr and 45 nm Au. For lift-off, the sample was soaked in Remover PG at 60°C for 10 min to remove the photoresist and then washed in isopropanol and DI water. Device characterization was performed using a semiconductor parameter analyzer (Keysight B1500A) and a Lakeshore cryogenic probe station with micromanipulation probes and liquid nitrogen cooling. All measurements were performed in vacuum ($<3 \times 10^{-6}$ torr).

SUPPLEMENTARY MATERIALS

Supplementary material for this article is available at http://advances.sciencemag.org/cgi/content/full/6/2/eaax8784/DC1

Fig. S1. Typical optical images of MoS_2 and Mo_5N_6 flakes with different thicknesses.
Fig. S2. Absorption spectra of MoS_2 and Mo_5N_6 samples on quartz substrate.
Fig. S3. AFM images of MoS_2 and Mo_5N_6 flakes in Fig. 2.
Fig. S4. PL intensity maps of MoS_2 and Mo_5N_6 flake.
Fig. S5. Structural and elemental characterizations of Mo_5N_6.
Fig. S6. TEM images of Mo_5N_6 sample under 200-keV electron beam.
Fig. S7. EDS spectrum of Mo_5N_6.
Fig. S8. Optical, AFM, and SEM images of chemical transformation on a four-layer MoS_2 flake.
Fig. S9. Optical images of Mo_5N_6 flakes prepared from chemical transformations under different conditions.
Fig. S10. Optical images and Raman spectra of a partially converted flake at 700°C.
Fig. S11. Stability test of Mo_5N_6, W_5N_6, and TiN.
Fig. S12. Optical and SEM images of WS_2, W_5N_6, TiS_2, and TiN flakes.
Fig. S13. Optical and AFM images of Mo_5N_6 transport device.
Fig. S14. TEM and EDS characterizations of W_5N_6 converted from WS_2.

REFERENCES AND NOTES

1. L. E. Toth, *Transition Metal Carbides and Nitrides* (Academic Press, 1971).
2. H. A. Pierson, *Handbook of Refractory Carbides and Nitrides* (Noyes, 1996).
3. M. Naguib, M. Kurtoglu, V. Presser, J. Lu, J. Niu, M. Heon, L. Hultman, Y. Gogotsi, M. W. Barsoum, Two-dimensional nanocrystals produced by exfoliation of Ti_3AlC_2. *Adv. Mater.* **23**, 4248–4253 (2011).
4. M. R. Lukatskaya, O. Mashtalir, C. E. Ren, Y. Dall'Agnese, P. Rozier, P. L. Taberna, M. Naguib, P. Simon, M. W. Barsoum, Y. Gogotsi, Cation intercalation and high volumetric capacitance of two-dimensional titanium carbide. *Science* **341**, 1502–1505 (2013).
5. B. Anasori, M. R. Lukatskaya, Y. Gogotsi, 2D metal carbides and nitrides (MXenes) for energy storage. *Nat. Rev. Mater.* **2**, 16098 (2017).
6. K. Hantanasirisakul, Y. Gogotsi, Electronic and optical properties of 2D transition metal carbides and nitrides (MXenes). *Adv. Mater.* **30**, 1804779 (2018).
7. P. Urbankowski, B. Anasori, T. Makaryan, D. Er, S. Kota, P. L. Walsh, M. Zhao, V. B. Shenoy, M. W. Barsoum, Y. Gogotsi, Synthesis of two-dimensional titanium nitride Ti_4N_3 (MXene). *Nanoscale* **8**, 11385–11391 (2016).
8. B. Soundiraraju, B. K. George, Two-dimensional titanium nitride (Ti_2N) MXene: Synthesis, characterization, and potential application as surface-enhanced raman scattering substrate. *ACS Nano* **11**, 8892–8900 (2017).
9. P. Urbankowski, B. Anasori, K. Hantanasirisakul, L. Yang, L. Zhang, B. Haines, S. J. May, S. J. L. Billinge, Y. Gogotsi, 2D molybdenum and vanadium nitrides synthesized by ammoniation of 2D transition metal carbides (MXenes). *Nanoscale* **9**, 17722–17730 (2017).
10. M. Naguib, O. Mashtalir, J. Carle, V. Presser, J. Lu, L. Hultman, Y. Gogotsi, M. W. Barsoum, Two-dimensional transition metal carbides. *ACS Nano* **6**, 1322–1331 (2012).
11. B. Anasori, Y. Xie, M. Beidaghi, J. Lu, B. C. Hosler, L. Hultman, P. R. C. Kent, Y. Gogotsi, M. W. Barsoum, Two-dimensional, ordered, double transition metals carbides (MXenes). *ACS Nano* **9**, 9507–9516 (2015).
12. A. Lipatov, M. Alhabeb, M. R. Lukatskaya, A. Boson, Y. Gogotsi, A. Sinitskii, Effect of synthesis on quality, electronic properties and environmental stability of individual monolayer Ti_3C_2 MXene flakes. *Adv. Electron. Mater.* **2**, 1600255 (2016).
13. F. Shahzad, M. Alhabeb, C. B. Hatter, B. Anasori, S. Man Hong, C. M. Koo, Y. Gogotsi, Electromagnetic interference shielding with 2D transition metal carbides (MXenes). *Science* **353**, 1137–1140 (2016).
14. Y.-Y. Peng, B. Akuzum, N. Kurra, M.-Q. Zhao, M. Alhabeb, B. Anasori, E. C. Kumbur, H. N. Alshareef, M.-D. Ger, Y. Gogotsi, All-MXene (2D titanium carbide) solid-state microsupercapacitors for on-chip energy storage. *Energ. Environ. Sci.* **9**, 2847–2854 (2016).
15. H. Jin, X. Liu, A. Vasileff, Y. Jiao, Y. Zhao, Y. Zheng, S.-Z. Qiao, Single-crystal nitrogen-rich two-dimensional Mo_5N_6 nanosheets for efficient and stable seawater splitting. *ACS Nano* **12**, 12761–12769 (2018).
16. L. H. Karlsson, J. Birch, J. Halim, M. W. Barsoum, P. O. Å. Persson, Atomically resolved structural and chemical investigation of single MXene sheets. *Nano Lett.* **15**, 4955–4960 (2015).
17. X. Sang, Y. Xie, M.-W. Lin, M. Alhabeb, K. L. Van Aken, Y. Gogotsi, P. R. C. Kent, K. Xiao, R. R. Unocic, Atomic defects in monolayer titanium carbide ($Ti_3C_2T_x$) MXene. *ACS Nano* **10**, 9193–9200 (2016).
18. L. Yu, Y.-H. Lee, X. Ling, E. J. G. Santos, Y. C. Shin, Y. Lin, M. Dubey, E. Kaxiras, J. Kong, H. Wang, T. Palacios, Graphene/MoS_2 hybrid technology for large-scale two-dimensional electronics. *Nano Lett.* **14**, 3055–3063 (2014).
19. Y.-C. Lin, B. Jariwala, B. M. Bersch, K. Xu, Y. Nie, B. Wang, S. M. Eichfeld, X. Zhang, T. H. Choudhury, Y. Pan, R. Addou, C. M. Smyth, J. Li, K. Zhang, M. A. Haque, S. Fölsch, R. M. Feenstra, R. M. Wallace, K. Cho, S. K. Fullerton-Shirey, J. M. Redwing, J. A. Robinson, Realizing large-scale, electronic-grade two-dimensional semiconductors. *ACS Nano* **12**, 965–975 (2018).
20. X. Li, W. Cai, J. An, S. Kim, J. Nah, D. Yang, R. Piner, A. Velamakanni, I. Jung, E. Tutuc, S. K. Banerjee, L. Colombo, R. S. Ruoff, Large-area synthesis of high-quality and uniform graphene films on copper foils. *Science* **324**, 1312–1314 (2009).
21. X. Ling, Y.-H. Lee, Y. Lin, W. Fang, L. Yu, M. S. Dresselhaus, J. Kong, Role of the seeding promoter in MoS_2 growth by chemical vapor deposition. *Nano Lett.* **14**, 464–472 (2014).
22. Z. Cai, B. Liu, X. Zou, H.-M. Cheng, Chemical vapor deposition growth and applications of two-dimensional materials and their heterostructures. *Chem. Rev.* **118**, 6091–6133 (2018).
23. S. T. Oyama, *The Chemistry of Transition Metal Carbides and Nitrides*, S. T. Oyama, Ed. (Blackie Academic and Professional, 1996).
24. C. Giordano, C. Erpen, W. Yao, M. Antonietti, Synthesis of Mo and W carbide and nitride nanoparticles via a simple "urea glass" route. *Nano Lett.* **8**, 4659–4663 (2008).
25. J. Liu, S. Tang, Y. Lu, G. Cai, S. Liang, W. Wang, X. Chen, Synthesis of Mo_2N nanolayer coated MoO_2 hollow nanostructures as high-performance anode materials for lithium-ion batteries. *Energ. Environ. Sci.* **6**, 2691–2697 (2013).
26. M. B. Sreedhara, K. Vasu, C. N. R. Rao, Synthesis and characterization of few-layer nanosheets of GaN and other metal nitrides. *Z. anorg. allg. Chemie.* **640**, 2737–2741 (2014).
27. G.-D. Sun, G.-H. Zhang, K.-C. Chou, Synthesis of molybdenum nitrides nanosheets by nitriding 2H-MoS_2 with ammonia. *J. Am. Ceram. Soc.* **101**, 2796–2808 (2018).
28. X. Xiao, H. Wang, P. Urbankowski, Y. Gogotsi, Topochemical synthesis of 2D materials. *Chem. Soc. Rev.* **47**, 8744–8765 (2018).
29. K. S. Novoselov, D. Jiang, F. Schedin, T. J. Booth, V. V. Khotkevich, S. V. Morozov, A. K. Geim, Two-dimensional atomic crystals. *Proc. Natl. Acad. Sci. U.S.A.* **102**, 10451–10453 (2005).
30. K. Kang, S. Xie, L. Huang, Y. Han, P. Y. Huang, K. F. Mak, C.-J. Kim, D. Muller, J. Park, High-mobility three-atom-thick semiconducting films with wafer-scale homogeneity. *Nature* **520**, 656–660 (2015).
31. S. D. Yim, S. J. Kim, J. H. Baik, I.-S. Nam, Y. S. Mok, J.-H. Lee, B. K. Cho, S. H. Oh, Decomposition of urea into NH_3 for the SCR process. *Ind. Eng. Chem. Res.* **43**, 4856–4863 (2004).
32. A. Lundström, B. Andersson, L. Olsson, Urea thermolysis studied under flow reactor conditions using DSC and FT-IR. *Chem. Eng. J.* **150**, 544–550 (2009).
33. A. Splendiani, L. Sun, Y. Zhang, T. Li, J. Kim, C.-Y. Chim, G. Galli, F. Wang, Emerging photoluminescence in monolayer MoS_2. *Nano Lett.* **10**, 1271–1275 (2010).

34. T. J. Wieting, J. L. Verble, Infrared and raman studies of long-wavelength optical phonons in hexagonal MoS_2. *Phys. Rev. B* **3**, 4286–4292 (1971).

35. J. L. Verble, T. J. Wieting, Lattice mode degeneracy in MoS_2 and other layer compounds. *Phys. Rev. Lett.* **25**, 362–365 (1970).

36. G. Eda, H. Yamaguchi, D. Voiry, T. Fujita, M. Chen, M. Chhowalla, Photoluminescence from chemically exfoliated MoS_2. *Nano Lett.* **11**, 5111–5116 (2011).

37. A. Garcia, A. M. Raya, M. M. Mariscal, R. Esparza, M. Herrera, S. I. Molina, G. Scavello, P. L. Galindo, M. Jose-Yacaman, A. Ponce, Analysis of electron beam damage of exfoliated MoS_2 sheets and quantitative HAADF-STEM imaging. *Ultramicroscopy* **146**, 33–38 (2014).

38. R. Zan, Q. M. Ramasse, R. Jalil, T. Georgiou, U. Bangert, K. S. Novoselov, Control of radiation damage in MoS_2 by graphene encapsulation. *ACS Nano* **7**, 10167–10174 (2013).

39. L. Zhang, X. Ji, X. Ren, Y. Ma, X. Shi, Z. Tian, A. M. Asiri, L. Chen, B. Tang, X. Sun, Electrochemical ammonia synthesis via nitrogen reduction reaction on a MoS_2 catalyst: Theoretical and experimental studies. *Adv. Mater.* **30**, 1800191 (2018).

40. C. Martella, P. Melloni, E. Cinquanta, E. Cianci, M. Alia, M. Longo, A. Lamperti, S. Vangelista, M. Fanciulli, A. Molle, Engineering the growth of MoS_2 via atomic layer deposition of molybdenum oxide film precursor. *Adv. Electron. Mater.* **2**, 1600330 (2016).

41. E. S. Kadantsev, P. Hawrylak, Electronic structure of a single MoS_2 monolayer. *Solid State Commun.* **152**, 909–913 (2012).

42. A. Y. Ganin, L. Kienle, G. V. Vajenine, Synthesis and characterisation of hexagonal molybdenum nitrides. *J. Solid State Chem.* **179**, 2339–2348 (2006).

43. F. Bonaccorso, Z. Sun, T. Hasan, A. C. Ferrari, Graphene photonics and optoelectronics. *Nat. Photonics* **4**, 611–622 (2010).

44. M. Thripuranthaka, R. V. Kashid, C. Sekhar Rout, D. J. Late, Temperature dependent Raman spectroscopy of chemically derived few layer MoS_2 and WS_2 nanosheets. *Appl. Phys. Lett.* **104**, 081911 (2014).

45. C. J. Carmalt, S. A. O'Neill, I. P. Parkin, E. S. Peters, Titanium sulfide thin films from the aerosol-assisted chemical vapour deposition of [Ti(SBu^t)$_4$]. *J. Mater. Chem.* **14**, 830–834 (2004).

46. C. C. Chen, N. T. Liang, W. S. Tse, I. Y. Chen, J. G. Duh, Raman spectra of titanium nitride thin films. *Chinese J. Phys.* **32**, 205 (1994).

47. S. Yu, Q. Zeng, A. R. Oganov, G. Frapper, L. Zhang, Phase stability, chemical bonding and mechanical properties of titanium nitrides: A first-principles study. *Phys. Chem. Chem. Phys.* **17**, 11763–11769 (2015).

48. Z. Zhao, K. Bao, D. Duan, F. Tian, Y. Huang, H. Yu, Y. Liu, B. Liu, T. Cui, The low coordination number of nitrogen in hard tungsten nitrides: A first-principles study. *Phys. Chem. Chem. Phys.* **17**, 13397–13402 (2015).

49. V. Grillo, E. Rotunno, STEM_CELL: A software tool for electron microscopy: Part I—Simulations. *Ultramicroscopy* **125**, 97–111 (2013).

Science Advances

Realization of 2D crystalline metal nitrides via selective atomic substitution

Jun Cao, Tianshu Li, Hongze Gao, Yuxuan Lin, Xingzhi Wang, Haozhe Wang, Tomás Palacios and Xi Ling

Use of this article is subject to the Terms of Service